New Journal of Physics
The open access journal for physics

Generation of high energy density by fs-laser-induced confined microexplosion

E G Gamaly[1,3], L Rapp[1], V Roppo[1], S Juodkazis[2] and A V Rode[1]

[1] Laser Physics Centre, Research School of Physics and Engineering, The Australian National University, Canberra, ACT 0200, Australia
[2] Swinburne University of Technology, Hawthorn, VIC 3122, Australia
E-mail: gam111@physics.com.au

New Journal of Physics **15** (2013) 025018 (19pp)
Received 18 September 2012
Published 11 February 2013
Online at http://www.njp.org/
doi:10.1088/1367-2630/15/2/025018

Abstract. Confined microexplosion produced by a tightly focused fs-laser pulse inside transparent material proved to be an efficient and inexpensive method for achieving high energy density up to several MJ per cm^3 in the laboratory table-top experiments. First studies already confirmed the generation of TPa-range pressure, the formation of novel super-dense material phases and revealed an unexpected phenomenon of spatial separation of ions with different masses in hot non-equilibrium plasma of confined microexplosion. In this paper, we show that the intense focused pulse propagation accompanied by a gradual increase of ionization nonlinearity changes the profile and spectrum of the pulse. We demonstrate that the motion of the ionization front in the direction opposite to the pulse propagation reduces the absorbed energy density. The voids in our experiments with fused silica produced by the microexplosion-generated pressure above Young's modulus indicate, however, that laser fluence up to 50 times above the ionization threshold is effectively absorbed in the bulk of the material. The analysis shows that the ion separation is enhanced in the non-ideal plasma of microexplosion. These findings open new avenues for the studies of high-pressure material transformations and warm dense matter conditions by confined microexplosion produced by intense fs-laser.

[3] Author to whom any correspondence should be addressed.

Contents

1. Introduction

The quest for recreating in laboratory experiments the high-pressure and high-temperature conditions which regulate the processes inside the stars and planets has been a driving force for researches for more than a century. It is now possible to obtain multi-megabar static pressure with simultaneous heating up to 3000 K by a laser pulse [1–3]. Extreme high-pressure/temperature transient conditions are created by the interaction of powerful laser pulses with the solid surface [4, 5].

The first notion that the extreme conditions produced in the ultrafast laser-driven confined microexplosion may serve as a novel microscopic laboratory for high-pressure and -temperature studies, well beyond the levels achieved in a diamond anvil cell, was presented by Glezer and Mazur in 1997 [6]. Recently, it was experimentally demonstrated that it is possible to create super-high-pressure and -temperature conditions in table-top laboratory experiments with ultrashort laser pulses focused inside transparent material to a level significantly above the threshold for optical breakdown [7–9]. The laser energy absorbed in a sub-micron volume confined inside a bulk of pristine solid is fully converted into the internal energy. Therefore high energy density, several times higher than the strength of any material, can be achieved with $\sim$100 fs, 1 μJ laser pulses focused down to a 1 μm^3 volume inside the solid.

There are several stages of the process affecting the magnitude of maximum energy density in the energy absorbing volume. We discuss first the processes accompanying the laser energy delivery through transparent material to a focal volume. The intensity of the focused pulse gradually increases, attaining optical breakdown threshold, which is achieved when the electron number density in the conduction band is equal to the critical density for the particular laser wavelength. Ionization nonlinearity of the solid material influences the beam structure and its

spectrum at lower intensity before the breakdown. After the breakdown, light is absorbed in the skin layer of plasma and energy absorption volume shrinks well below the focal volume, thus increasing the energy density. For example, a ∼100 fs laser pulse with ∼100 nJ energy tightly focused to a micron-size focus below the surface produces the energy density of several MJ per cm^3 in a sub-micron volume, higher than the strength of any material. The confined plasma then explodes and generates a powerful shock wave that expands out of the absorbing volume, compresses the surrounding pristine material and finally decays inside the bulk [7–9]. The pressure driving the shock wave reaches the magnitude of several TPa, triggering dramatic changes in the compressed material properties. The essential distinctive feature of laser-driven microexplosion is that the modified material remains compressed and confined in a strongly localized region inside a bulk, and can be investigated later.

First microexplosion experiments were performed with sapphire, silica, polystyrene [7–9] and recently germanium oxide [10]. There was a preliminary conjecture put forward that phase separation in silica can be the reason for the observed alterations in O–O and Si–Si pair correlations [11]. Synchrotron x-ray diffraction microanalysis of the compressed shell in sapphire demonstrated that a new stable high-pressure phase, a bcc-Al, was formed by ultrafast microexplosion and confined inside sapphire α-Al_2O_3 [12]. The formation of a new phase of aluminium within the compressed sapphire provides evidence of an unusual and unexpected phenomenon, namely the spatial separation of Al- and O-ions at the plasma stage and then freezing the bcc-Al nanocrystals during the transition to ambient conditions [12]. It should be noted that the stoichiometry of aluminium oxide is preserved in the conditions of complete confinement and the absence of cracks around the void. The analysis reveals that spatial separation of ions with different masses is possible in highly non-equilibrium, hot, dense and short-lived plasmas, where the temperatures of electrons and ion species are significantly different.

In this paper, we extended the studies of microexplosion into the detailed analysis of the laser energy delivery to the focal spot buried deep under the surface aiming to maximize the concentration of energy density in the bulk of the material. We describe the processes involved in the energy delivery to the focal spot by the converging laser pulse with increasing intensity. We demonstrate the effect of ionization wave propagation towards the laser pulse with increased laser intensity limiting the energy density deposited into the material. On the basis of these considerations, we formulate the criteria for optimal focusing of intense femtosecond laser pulses into transparent dielectrics to maximize the energy volume density. We consider the processes of ionization, absorption, formation of the shock and rarefaction waves and creation of void. Special attention is paid to the structure of the shock wave in hot non-ideal plasma. We discuss this mechanism of spatial separation of ions with different masses in details. We conclude and indicate future directions and applications of laser-driven microexplosion in the final section.

2. Succession of important processes

The first experiments and detailed description of major processes accompanying confined microexplosion in a single material crystal are described in [7–9]. In this paper, we concentrate on the recent results uncovering the details in previously studied phenomena and describing other important effects. These effects include spectral and spatial changes in the pulse profile, and the expansion of ionization wave in the direction towards the pulse propagation.

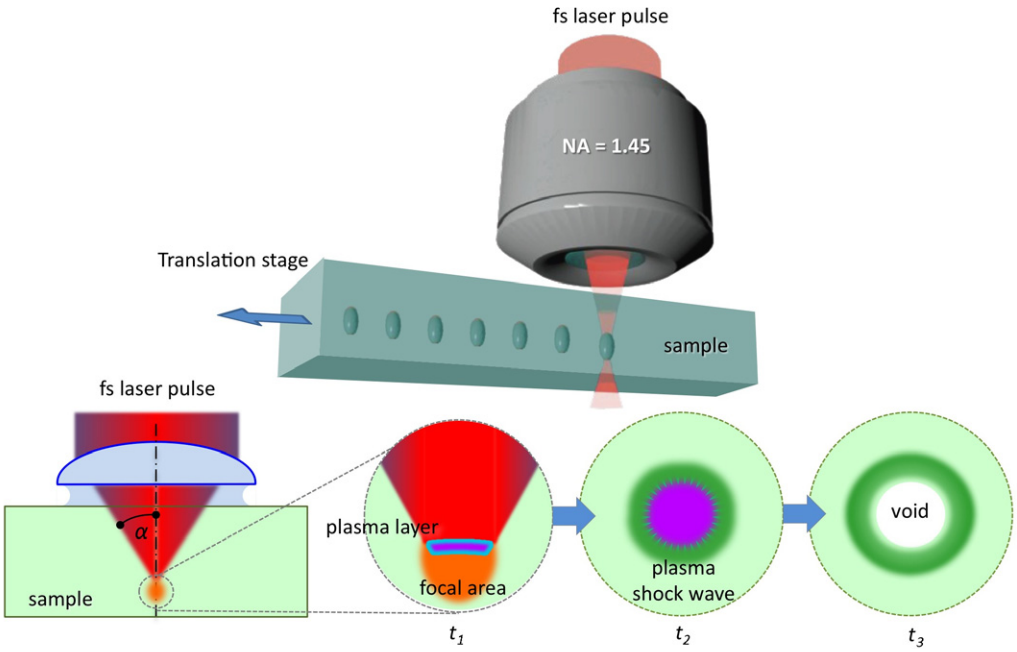

Figure 1. Schematic representation of the experiments and the processes in fs-laser-induced microexplosion inside transparent dielectric. Three blown-up focal areas are shown in time sequences $t_1 < t_2 < t_3$. The first time slot t_1 during the pulse ~170 fs shows the formation of the energy absorbing plasma layer inside the focal area; the second interval $t_2 \sim$ 1–100 ps shows hydrodynamic expansion of plasma and the formation of a shock wave; the third $t_3 \sim$ 100 ps–1 ns shows rarefaction wave, and the formation of a void surrounded by a densified shell due to quenching.

It is instructive to start with the scheme of the experimental setup for confined microexplosion and the stages of material transformation (figure 1).

The problem of confined microexplosion naturally splits into two interconnected problems describing two major stages with different time scales. At the first stage during the sub-picosecond pulse time, we consider beam propagation to the focal spot, and light absorption in the plasma formed from the moment when the optical breakdown is reached to the end of the laser pulse. At the second stage, which proceeds mainly after the pulse, the absorbed energy transfers from electrons to the ions generating the shock and rarefaction waves, compression of material and formation of voids. This stage continues up to a few nanoseconds. We will start with the beam propagation and absorption.

3. Energy delivery inside a transparent solid

The laser beam is focused with a high-numerical aperture (NA) microscope lens at depths typically from ~5 μm to 50 μm under the surface. The converging powerful laser beam with intensity changing in space and in time propagates inside the transparent crystal at depths largely exceeding the laser wavelength and the focal spot size. In order to achieve the highest possible absorbed energy density in the focal region for a given pulse energy, the energy losses during the beam energy delivery should be minimized.

The first restriction is set on the power of the laser beam, which should be less than the critical power for self-focusing in a crystal, $P < P_{cr} = 0.93\,\lambda_0^2/(2\pi\, n_0 n_2)$, where λ_0 is the laser wavelength, n_0 is the linear and n_2 is the nonlinear parts of refractive index ($n = n_0 + n_2 I$) of a medium for the Gaussian beam [9]. The intensity at the focal spot gradually increases during the pulse and the absorbed energy density reaches the ionization threshold. At this threshold the real part of the dielectric function turns from the positive to the negative range, the laser wave becomes evanescent and the laser energy is absorbed in plasma in a volume of a skin layer which is much less than the focal volume. The breakdown threshold is defined by the condition that the number density of excited electrons in the spatial point r, z reaches the critical density value:

$$n_c = \int_0^{t_{ion}} W(I(r, z, t))\,\mathrm{d}t, \tag{1}$$

where $W(I(x, t))$ is the sum of ionization rates from the ionization by electron impact and multi-photon mechanisms. The time from the leading front edge to the moment when the number density of electrons in the conduction band reaches the critical density, $n_e = n_{cr}$, $n_{cr} = m_e\omega^2/4\pi e^2$, defines the ionization time t_{ion}. The energy of the propagating beam decreases due to the losses for electron excitation, ionization and absorption, resulting in changes in the amplitude of the transient field.

There are several effects of the transient ionization on the beam propagation known from the studies of laser-induced breakdown of gases ([13], see review [14] and references therein), which affect the absorbed energy density. The laser spectrum shifts to the blue side; the group velocity of the pulse becomes intensity dependent. As a result, the front of the pulse steepens slightly shortening the pulse [14]. After the ionization threshold the boundary of the volume, where the breakdown is achieved, is moving during the pulse in the direction opposite to the laser beam propagation [13]. We discuss these effects in more detail later in the paper.

3.1. Formulation of the problem

The complete problem of microexplosion should be described by a set of Maxwell equations coupled to those for the ionization, and for the energy, momentum and angular momentum conservation. The paraxial approximation is inapplicable for this task because the changes in the dielectric function and wave vector are comparable with the unperturbed values.

The set of equations for the description of the propagation of powerful laser beams inside a crystal is as follows:

$$\begin{cases} \nabla \times \nabla \times E = -\dfrac{1}{c^2}\dfrac{\partial^2 D}{\partial t^2}, \quad D = \varepsilon E, \\ \operatorname{div} D = 0, \\ \varepsilon = \varepsilon_{pol} + \mathrm{i}\dfrac{4\pi\sigma}{\omega} = \varepsilon_{re}(n_e) + \mathrm{i}\varepsilon_{im}(n_e), \\ \dfrac{\partial n_e}{\partial t} = W(I(r, z, t)) - R(r, z, t), \\ \dfrac{\partial E_e}{\partial t} = Q_{abs} - Q_{e\text{-}ph}, \\ \dfrac{\partial E_L}{\partial t} = Q_{e\text{-}ph}, \end{cases} \tag{2}$$

where E_e and E_L are the energy density of electrons and lattice, $Q_{e\text{-}ph}$ is the energy transfer from electrons to lattice and later to ions, $W(I(x,t))$ is the sum of ionization rates from electron impact (avalanche) and multi-photon mechanisms; the term $R(r,z,t)$ accounts for the recombination. The energy losses due to the electron heat conduction during the beam propagation time can be neglected. These losses along with the momentum conservation equations are considered at the explosion stage when the heat wave and ion motion are essential.

The light beam with the pulse duration, t_p, and with the initial diameter, d_0, at the vacuum–solid boundary propagates in a medium with the initial refractive index n with the group velocity c/n. For example, at the low intensity light propagates a distance of 10 μm in the unperturbed fused silica ($n = 1.5$) during 50 fs. This time has to be taken into account when considering the time for ionization time the maximum intensity delivered to the focus.

The beam is focused at a distance L_f inside a medium to the diameter, d_f, smaller than the laser wavelength, λ_0, $d_f < \lambda_0 < d_0$, with a microscope and high-numerical aperture (NA) lens, $\mathrm{NA} = n \sin\alpha$ (see figure 1), where α is the half-converging angle. The beam radius at the entrance to a medium, r_0, reads $r_0 = L_f \operatorname{tg}\alpha$. Let us consider, for example, a 800 nm laser beam focused with NA = 1.4 through the immersion oil as a refractive index matching the liquid into a fused silica ($n = 1.5$) sample at the depth $L_f = 10\,\mu$m to the focal spot with radius $r_f = 0.5\,\mu$m. One obtains $\sin\alpha = 0.933 (\alpha = 75.17^\circ; \operatorname{tg}\alpha = 3.777)$. The beam radius decreases from $r_0 = 37.77\,\mu$m to $r_f = 0.5\,\mu$m at the depth of 10 μm, the intensity at the focus increases in $(r_0/r_f)^2 = 5706$ times. Taking the laser power of 2.5 MW (250 nJ in 100 fs) below the critical for self-focusing (for silica $P_{cr} = 3$ MW) one obtains the intensity at the focus $I_f = 6.37 \times 10^{14}\,\mathrm{W\,cm^{-2}}$ and at the surface $I_0 = 1.12 \times 10^{11}\,\mathrm{W\,cm^{-2}}$. Thus, a 100 fs laser pulse with 250 nJ is appropriate for such experiments as was already demonstrated [7–12].

It was experimentally established that the critical electron density in fused silica generated by a 800 nm laser pulse takes 160 fs at the intensity of $1.17 \times 10^{13}\,\mathrm{W\,cm^{-2}}$ [21]. It should be stressed here that the ionization threshold is an integral characteristic, see equation (1), depending on the ionization time and on the time-dependent intensity that defines the ionization rates. Therefore, the ionization threshold is defined by both the energy deposited and the time required for ionizing the material to the critical electron density, and as a result by the fluence, $F_{thr} = (1.17 \times 10^{13}\,\mathrm{W\,cm^{-2}} \times 160\,\mathrm{fs}) = 1.87\,\mathrm{J\,cm^{-2}}$, and not by a single instantaneous intensity value only, as presented in many papers (see, e.g., [15]).

3.2. Dependence of the dielectric function on laser intensity: effects of polarization and ionization

Let us express the dielectric function in equation (2) as a sum of polarization term and change due to ionization in the Drude-like form. It is instructive measuring the electron number density in units of the critical density, $n_{cr} = m_e\omega^2/4\pi e^2$, introducing the dimensionless density, $\rho_e = n_e/n_{cr}$, as the following:

$$\varepsilon \approx \varepsilon_{pol} - \rho_e \left(1 + \frac{\nu_{ei}^2}{\omega^2}\right)^{-1} + \mathrm{i}\rho_e \left(1 + \frac{\nu_{ei}^2}{\omega^2}\right)^{-1} \frac{\nu_{ei}}{\omega}, \tag{3}$$

where ω is the laser frequency; ν_{ei} is the electron effective collision frequency, which is close to its upper natural limit of $\nu_{ei} \cong \nu_e n_a^{1/3}$ near the plasma formation threshold; here n_a is the atomic number density and $v_e = (3\pi^2)^{1/3}\hbar\, n_e^{1/3} m_e^{-1}$ is the electron velocity. At the leading edge of the pulse when the laser intensity is low and the level of ionization is negligible, the dielectric

function grows up due to the Kerr effect, $\varepsilon_{\rm pol} \approx \varepsilon_0 + 2n_2\,\varepsilon_0^{1/2} I$. It is also worth noting that the Kerr coefficient is inversely proportional to the temperature $\Delta\varepsilon_{\rm Kerr} \propto E^2/k_{\rm B}T$ [16]. Therefore, the small initial increase in dielectric function with growing intensity will be compensated for by the increase in temperature and then will be prevailed by the negative contribution from increasing the ionization. For fused silica $n_2 \approx 10^{-16}\,{\rm cm^2\,W^{-1}}$. Therefore even at the intensity of over $10^{14}\,{\rm W\,cm^{-2}}$ this contribution is small. However, it was indicated [16] that at some elevated intensity the separation on the polarization and ionization parts is physically illegible. Therefore, the dielectric function should take a general form, $\varepsilon = 1 + 4\pi\chi$, where susceptibility includes all contributions from the bonded electrons, from free electrons and magnetic effects.

Let us estimate the changes of dielectric function near the critical density in fused silica as an example. The atomic number density in silica is $n_{\rm a} = 2.1 \times 10^{22}\,{\rm cm^{-3}}$, while the critical density at 800 nm ($\omega = 2.356 \times 10^{15}\,{\rm s^{-1}}$) is equal to $n_{\rm cr} = 1.74 \times 10^{21}\,{\rm cm^{-3}}$. Thus one obtains, for the velocity of electrons in the conduction band, $v_{\rm e}(n_{\rm cr}) = 4.82 \times 10^7\,{\rm cm\,s^{-1}}$ and the effective electron collision rate, $\nu_{\rm ei}(n_{\rm cr}) = 1.33 \times 10^{15}\,{\rm s^{-1}}$. At the critical density, the real and imaginary parts of the Drude contribution are correspondingly $\varepsilon_{\rm re}^{\rm (D)} \sim -0.68$ and $\varepsilon_{\rm im}^{\rm (D)} \approx 0.43$. It is reasonable to suggest that the first term in equation (3) is equal to 1 in accord with the general recipe. Respectively, the real and imaginary parts of the dielectric function at the ionization front are $\varepsilon_{\rm re} = 0.32$ and $\varepsilon_{\rm im} = 0.43$ giving for refractive index $n = 0.605$ and $\kappa = 0.355$, which is significantly different from the values of unperturbed fused silica of $n = 1.45\kappa \sim 10^{-6}$. The Fresnel absorption coefficient is $A = 0.9$ and the absorption length $l_{\rm abs} \approx c/k\omega \sim 0.356\,\mu{\rm m}$. One can see that the absorbed energy density at the fluence corresponding to the breakdown threshold in silica, $E_{\rm abs} = 2AF_{\rm th}/l_{\rm abs} \cong 9.45 \times 10^5\,{\rm J\,cm^{-3}}$, which indicates multiple ionization of the absorbing volume of the plasma skin layer.

3.3. Rate equation for electron generation: ionization mechanisms, thresholds and rates

It is well established that in the intensity domain of 10^{14}–$10^{15}\,{\rm W\,cm^{-2}}$ the ionization by the electron impact and multi-photon ionization are the dominating ionization mechanisms [13, 17]. The magnitude of the adiabaticity parameter combining field and material properties allows separating the different ionization regimes in a strong electromagnetic field, $\gamma^2 = J_{\rm i}/\varepsilon_{\rm osc}$ (here $J_{\rm i}$ is the ionization potential and $\varepsilon_{\rm osc}$ is the energy of electron oscillations in the field E, $\varepsilon_{\rm osc} = e^2E^2/4m_{\rm e}\omega^2$) [17]. It is convenient to express this parameter through the laser intensity of the linearly polarized high-frequency electric field averaged by many laser periods, $I = cE^2/8\pi$. For practical use we express the adiabaticity parameter through the laser intensity in units of $10^{14}\,{\rm W\,cm^{-2}}$ and the wavelength in microns as the following [16]: $\gamma^2 = 1.45/I\,\lambda^2$; we take here, $\varepsilon_{\rm osc}\,({\rm eV}) = 9.31 \times I\lambda^2$. The value $\gamma = 1$ separates the multi-photon ($\gamma > 1$) and tunnelling regimes ($\gamma < 1$). In experiments with $\lambda = 0.8\,\mu{\rm m}$ and $I = 10^{14}$–$10^{15}\,{\rm W\,cm^{-2}}$. We take the field ionization rate in the transitional region, as generally accepted, in the multi-photon form.

3.3.1. Multi-photon ionization rate. In order to simplify the rate equation we take the multiphoton ionization rate (MPI) in its limiting form ($\gamma \gg 1$) [13]:

$$w_{\rm mpi} \propto \omega\,\lambda^{2n_{\rm ph}} n_{\rm ph}^{3/2} \left(\frac{9.31}{\Delta_{\rm g}}\right)^{n_{\rm ph}} \left(\frac{I}{10^{14}}\right)^{n_{\rm ph}},$$

where $n_{\rm ph}$ is the number of photons necessary for freeing one electron, $n_{\rm ph} = (J_{\rm i} + \varepsilon_{\rm osc})/\hbar\omega \approx J_{\rm i}/\hbar\omega$; λ is expressed in μm, the band gap $\Delta_{\rm g}$ is in eV and the intensity I is in ${\rm W\,cm^{-2}}$.

For dielectrics one should replace the ionization potential by the band gap, $J_i \approx \Delta_g$. The energy of free electron is $\varepsilon_e = n_{ph}\hbar\omega - \Delta_g$. We take the multi-photon rate for a single atom in fused silica suggesting that five photons is necessary for stripping one electron following [18, 19]

$$w_{mpi} = \beta_{n_{ph}} I^{n_{ph}}, \quad \beta_5 = 1.3 \times 10^{-55}\,\mathrm{cm^2\,W^{-1}\,s^{-1}}. \tag{4}$$

It was calculated in [18] that the critical density for the combined avalanche and MPI mechanisms in fused silica with the Gaussian pulse shape and peak intensity of $1.17 \times 10^{13}\,\mathrm{W\,cm^{-2}}$ was reached at 160 fs.

3.3.2. Electron impact (avalanche) ionization rate. The energy of the electron's oscillations in the laser field was converted into its kinetic energy via collisions. The ionization by the electron impact develops into the avalanche process when the kinetic energy of the free electron exceeds the band gap. In general, the Keldysh impact formula should be applied, $w_{av} = w_{imp}\,(\varepsilon_{el}/\Delta_g - 1)^2$. The avalanche rate in the most general form is expressed as [13]

$$w_{imp} \approx \ln 2(\varepsilon_{osc}/\Delta_g)\nu_{eff}, \quad \nu_{eff} = \omega^2\nu_{ei}/(\omega^2 + \nu_{ei}^2). \tag{5}$$

For practical use it is convenient to present the rate proportional to the laser intensity with the proportionality coefficient depending on laser and material parameters in accord with equation (5):

$$w_{imp} = \alpha\, I \quad \left(\mathrm{s^{-1}}\right). \tag{6}$$

We take $\alpha = 10\,\mathrm{cm^2\,J^{-1}}$, which fits to the experiments in accord with [18, 19].

3.3.3. Rate equation for the electron number density. Summing up the results of sections 3.3.1 and 3.3.2 the rate equation for the electron number density can be presented in the form

$$\frac{\partial n_e}{\partial t} = w_{imp} n_e + w_{mpi}\,(n_a - n_e) - R, \tag{7}$$

where n_a is the atomic number density in the medium. The saturation of electron density after the single ionization is suggested in the MPI term.

It is known that in the hot and dense plasmas the recombination by three-body collisions dominates [20] with one electron acting as a third body. The recombination time is of the order of femtoseconds [9]. Therefore, the ionization equilibrium establishes early during the pulse time and the ionization state after the pulse can be found after the solution of the Saha equations, as was done for silica in conditions of confined microexplosion [9].

3.4. Effects of ionization on the spectrum, group velocity and diffraction of the propagating beam

The change in the real part of susceptibility due to the ionization nonlinearity has a negative sign (in contrast to the Kerr nonlinearity). Therefore the first effect of ionization is defocusing of the propagating beam. Other ionization effects, the modification of the pulse spectrum and its group velocity, were found in the studies of interaction of a short intense laser pulse with gases, where these effects are strong, see the review [14] and references therein. These effects can be qualitatively understood from a simple reasoning. Indeed, let us simplify the general dispersion

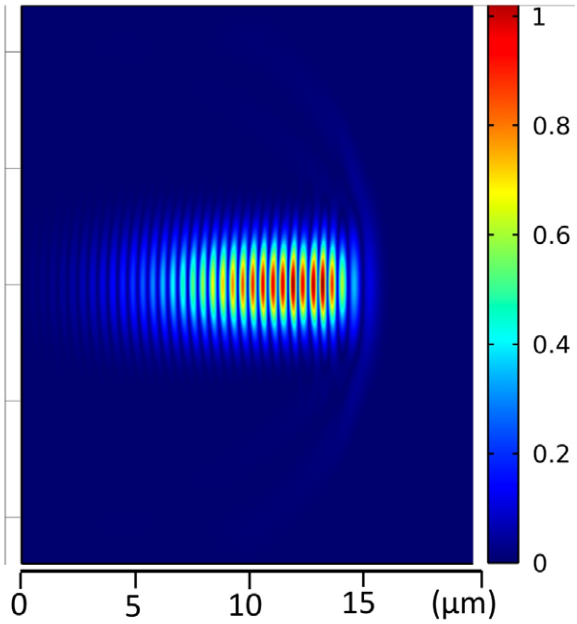

Figure 2. Snapshot of the electric field spatial distribution for a 25 fs pulse propagating at 10 μm depth into silica (the zero is at the surface). The central part of the pulse is overcoming the front edge due to intensity-dependent group velocity.

relation, $k^2c^2 = \varepsilon\,\omega^2$, leaving only the ionization effect and neglecting absorption to the form

$$\omega^2 \approx k^2c^2 + \omega_{\mathrm{pe}}^2, \tag{8}$$

where $\omega_{\mathrm{pe}}^2 = 4\pi\, e^2 n_{\mathrm{e}}/m_{\mathrm{e}}$ is the electron plasma frequency and k is the wave vector; we assume here a spectral bandwidth-limited pulse duration. The change in the group velocity, $v_{\mathrm{g}} = \mathrm{d}\,\omega/\mathrm{d}\,k$, under the assumption that changes are small, immediately follows:

$$\Delta v_{\mathrm{g}} = \frac{c^2\omega_{\mathrm{ope}}^2}{\omega_0^2 v_{0\mathrm{g}}}\left(\frac{\Delta\omega}{\omega} - \frac{\Delta n_{\mathrm{e}}}{n_{0\mathrm{e}}}\right). \tag{9}$$

Respectively, the change in frequency after the beam passes a distance L_{f} in the linear approximation reads

$$\Delta\omega \approx \frac{L_{\mathrm{f}}}{2\omega_0 v_{0\mathrm{g}}}\frac{\mathrm{d}\omega_{\mathrm{pe}}^2}{\mathrm{d}t} = \frac{L_{\mathrm{f}}\omega_0}{2v_{0\mathrm{g}}n_{\mathrm{cr}}}\frac{\mathrm{d}n_{\mathrm{e}}}{\mathrm{d}t}. \tag{10}$$

Thus the frequency is blue-shifted. Due to the strong nonlinear growth in electron density at the leading edge of the pulse ($\Delta\omega/\omega \sim \mathrm{d}n_{\mathrm{e}}/\mathrm{d}t) > \Delta n_{\mathrm{e}}/n_{0\mathrm{e}}$ the group velocity increases, leading to a pulse shortening as was observed in the experiments with gases (see, e.g., the review [14]).

This effect was observed in the numerical solution of three-dimensional Maxwell equations of the equation set (2) in the silica (see figure 2). The Maxwell equations were complemented by the rate equations for the generation of electrons due to multiphoton and avalanche processes at an intensity well below the breakdown threshold. However, the intensity was large enough for ionization nonlinearity to dominate the Kerr nonlinearity. As expected the effect in a solid is

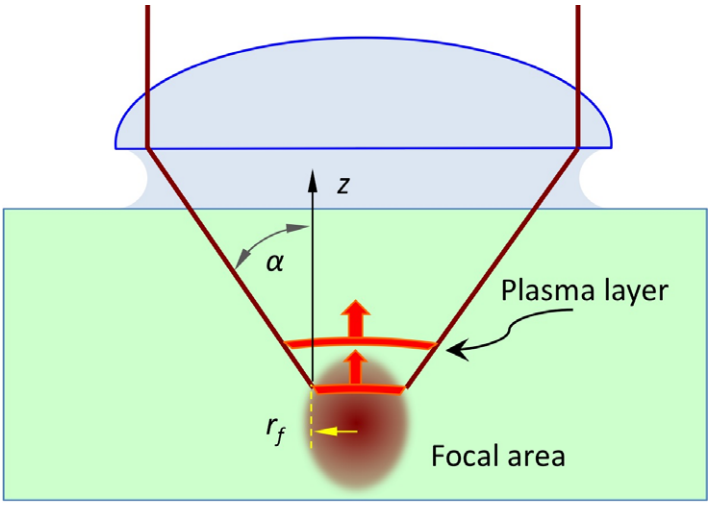

Figure 3. Scheme of the path of the converging focused beam as a truncated cone. The motion of the ionization front towards the beam propagation is indicated by the arrows.

much weaker than in gases. However, after the initial fast growth the second term in equation (9) prevails and the group velocity starts decreasing and goes to zero at the breakdown point.

3.5. Motion of the ionization front opposite to the beam direction

Another effect of ionization discovered in studies of the breakdown of gases is the motion of the ionization front in the direction opposite to the laser beam [13]. Indeed, the intense beam with the total energy well above the ionization threshold reaches the threshold value early in the beginning of the pulse. Laser energy increases and the beam cross-section where the laser fluence is equal to the threshold value, the ionization front, starts moving in the direction opposite to the beam direction. The beam is focused to the focal spot area, $S_\mathrm{f} = \pi r_\mathrm{f}^2$. The spatial shape of the beam path is a truncated cone, the intensity at any time to be independent of the transverse coordinates (see figure 3).

The ionization time, i.e. the time required for generating the number of electrons to reach the critical density in the conduction band, is defined by equation (1). Therefore, the threshold fluence is achieved at the beam cross-section with a radius increasing as the following:

$$r(z,t) = r_\mathrm{f} + z(t)\,\mathrm{tg}\,\alpha, \tag{11}$$

where z is the distance from the focal spot, which is supposed to be a circle with radius r_f (figure 2). Then at any moment t during the pulse the relation holds:

$$\frac{E_\mathrm{las}(t)}{\pi r^2(z,t)} = F_\mathrm{thr}. \tag{12}$$

We introduce the dimensionless parameter, $f = E_\mathrm{las}\left(t_\mathrm{p}\right)/\pi r_\mathrm{f}^2 F_\mathrm{thr} = F_\mathrm{las}/F_\mathrm{thr}$, as the ratio of the maximum fluence to the threshold fluence. Then the ionization front moved the distance $z(t_\mathrm{p})$:

$$z(t_\mathrm{p}) = \frac{r_\mathrm{f}}{\mathrm{tg}\,\alpha}(f^{1/2} - 1). \tag{13}$$

Correspondingly, the ionization time can be evaluated as

$$t_{\rm ion} = t_{\rm p}\left[1 - \left(1 - \frac{1}{f}\right)^{1/2}\right]. \tag{14}$$

One can see that if the total fluence is equal to that for the threshold, $f = 1$, the $n_{\rm cr}$ is reached only at the end of the pulse [18, 19, 21], the ionization time is equal to the pulse duration and thus there is no movement of the ionization front. These simple geometrical considerations are in qualitative agreement with the experiments in sapphire and silica, and in the experiments presented in section 6 further in the paper. Indeed, the voids measured in sapphire and in silica in [7–10] are slightly elongated; equation (13) gives $z_{\rm m} = 0.67 r_{\rm f}$ and $0.45 r_{\rm f}$ for sapphire and silica, respectively.

Summing up the results of this section, the effects of the blue shift of the pulse spectrum and the intensity dependence of the group velocity are small and rather positive for achieving high absorbed energy density. The negative effect of the ionization front motion at the laser energy well above the ionization threshold leads to a large decrease in the absorbed energy density. The negative effect of defocusing needs further careful studies with the solution of the Maxwell equations.

4. Absorbed energy density and the plasma state in the absorption volume

The electron temperature to the end of the pulse reaches a few tens of eV while the energy exchange time and the heat conduction time are both in the picosecond range. The ionization by electron impact continues after the end of the pulse resulting in approximately $Z = 4$–5 degree of ionization of the constituent atoms [7–9]. The shape and magnitude of the energy absorption volume cannot be measured or calculated with sufficient accuracy. To estimate the absorbed energy density and the plasma state, it is reasonable to follow the calculations of [9].

Conversion of the absorption region into hot and dense plasma dramatically reduces the energy deposition volume and correspondingly massively increases the absorbed energy density. The electron number density reaches $n_{\rm e} \cong 3 \times 10^{23}\,{\rm cm}^{-3}$, the electron–ion momentum exchange rate becomes comparable with the plasma frequency, and both are significantly higher than the laser frequency, $\nu_{\rm ei} \cong \omega_{\rm pe} \cong 2 \times 10^{16}\,{\rm s}^{-1} \gg \omega$. Thus, the real and imaginary parts of refractive index in such a plasma $n \cong \kappa \cong 2$, giving the absorption coefficient $A \cong 0.6$ and the absorption length $l_{\rm abs} \cong 6 \times 10^{-6}\,{\rm cm}$. Now the absorbed energy density reads $E_{\rm abs} = 2A\,F/l_{\rm abs} = 5 \times 10^5\,F_{\rm las}\,({\rm J\,cm}^{-3})$, where $F_{\rm las}$ is the laser fluence at the focal spot. One can see that delivering the fluence in excess, the ionization threshold of $\sim 2\,{\rm J\,cm}^{-2}$ to the focal spot inside silica creates energy density of the order of MJ per cm^3, or pressure $\sim 10^{12}$ Pa, and the energy per electron, $E_{\rm abs}/n_{\rm e}$, of a few tens of eV. Thus, we assume that the absorption volume in a cylinder is $V_{\rm abs} = \pi\, r_{\rm foc}^2\, l_{\rm abs} \cong 2.72 \times 10^{-14}\,{\rm cm}^3$, which we approximate by an equivalent sphere with radius $r_{\rm eff} = 0.254\,\mu{\rm m}$ we will use for the estimates in the next section.

5. Shock wave formation and the wave structure

Spatial separation of Al- and O-ions formation of bcc-Al nanocrystals has recently been discovered in the experiments on microexplosion in crystalline sapphire (Al_2O_3) [12]. The separation is due to the process of energy exchange and temperature equilibration in the multi-component plasma. Let us consider the energy exchange processes in more detail. We consider

below the two-component plasma containing light, M_l, and heavy, M_h, ions. The concentration of the laser energy in the absorption volume reaches several MJ per cm^3. The material in this volume is fully dissociated and both atoms (we consider crystal Al_2O_3 or amorphous fused silica SiO_2, $M_h^{Al} = 27$; $M_h^{Si} = 28$; $M_l^O = 16$) are multiple-ionized up to the degree $Z = 3$–5 by the end of the laser pulse [7–9]. The entire absorbed energy is contained in the electron component. The wave of electronic heat conduction starts to propagate into the surrounding material at the end of the pulse. The maximum electron temperature is estimated to be in the range of ~30–50 eV, taking into account the ionization losses. We take the momentum transfer rate for the ideal plasma in the approximate form, which reproduces the natural maximum that is close to $\omega_{pe} \sim 2 \times 10^{16}\ s^{-1}$ at the temperature of 10 eV:

$$\nu_{ei}^{mom} \cong \frac{2 \times 10^{16}}{(k_B T_e/10\,\mathrm{eV})^{3/2}}. \tag{15}$$

However, the departure from the ideal plasma description might be significant in the hot and dense plasma. The measure for such a departure is the number of particles in the Debye sphere, $N_{De} = 4\pi\, n_e\, \lambda_{De}^3/3$, where the Debye screening radius is $\lambda_{De} = (3k_B T_e/4\pi\, n_e e^2)^{1/2}$. At the temperature maximum one obtains $\lambda_{De} \sim 10^{-8}$ cm, $N_{De} \sim 1$ provided that the plasma is in a non-ideal state, and that at the cooling stage it departs further away from the ideal conditions into a strongly coupling non-ideal plasma. It is known [22] that in non-ideal plasma momentum, the exchange rate decreases in comparison with that for the ideal plasma as the following:

$$\frac{\nu_{ei}^{mom}}{\omega_{pe}} \approx \frac{Z \ln \Lambda}{10 N_{De}}, \tag{16}$$

where $\ln \Lambda$ is the Coulomb logarithm. Using the closest distance approach, one can estimate the Coulomb logarithm as the following: $\Lambda \approx 3N_{De}/Z$. Thus, in the conditions of confined microexplosion the electron–ion momentum exchange rate decreases in comparison with that for the ideal plasma approximately for several (up to ten) times. Therefore, we take this rate as $\nu_{non\text{-}ideal}^{mom}(s^{-1}) \cong 5 \times 10^{15}(k_B T_e/10\,\mathrm{eV})^{-3/2}$. Then the diffusion coefficient D_e for the electronic heat conduction reads [22]

$$D_e\ (\mathrm{cm^2\,s^{-1}}) = \frac{v_e^2}{3\,\nu_{non\text{-}i}^{mom}} = 2.67 \times \left(\frac{k_B T_e}{10\,\mathrm{eV}}\right)^{5/2}, \tag{17}$$

where we take $v_e^2 \approx 4 \times 10^{16}\,(k_B T_e/10\,\mathrm{eV})$. The rate of the energy transfer, ν_{ei}^{en}, from electrons to the ion of mass M_i reads $\nu_{ei}^{en} = \nu_{ei}^{mom} m_e/M_i$. The light ions gain the energy during the time $t_l\,(s) \cong 2 \times 10^{-16}(M_l/m_e)\,(k_B T_e/10\,\mathrm{eV})^{3/2}$ earlier than the heavy ones. For oxygen, the light ion in our experiments, with sapphire and silica, this time is $t_O\,(ps) \cong 5.84\,(k_B T_e/10\,\mathrm{eV})^{3/2}$. However, the heat wave carries the energy away from the absorption region during the energy transfer, resulting in the decrease of temperature. The time dependence of the heat wave front position and the temperature at the front can be estimated from the energy conservation and the nonlinear heat wave equation in the form

$$\begin{cases} \dfrac{(r - r_0)^2}{t} = D_e, \\ T_e\, r^3 = T_0\, r_0^3. \end{cases} \tag{18}$$

Here we assumed that the absorption volume is a sphere with the effective radius defined above. The heat wave expands outside of the surface of a homogeneously heated sphere. Then the

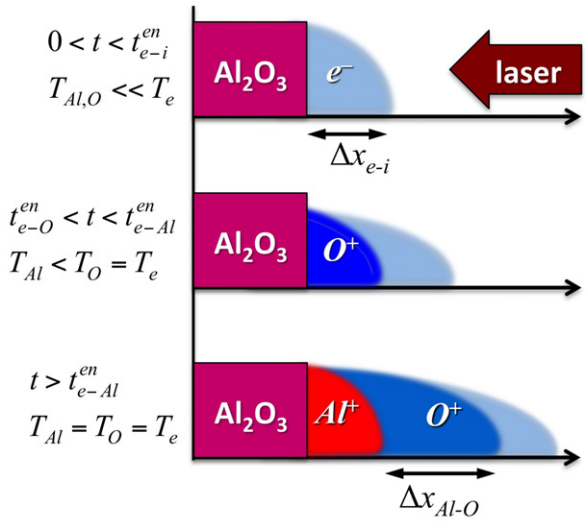

Figure 4. Structure of the shock wave front in the two-component plasma of aluminium and oxygen ions formed in sapphire at three time intervals after the pulse. The first shows the electronic heat wave propagation before the electron–ion energy equilibration, the second is after the electron–oxygen but before the electron–aluminium energy equilibration, and the third is after complete temperature equilibration (see the text for spatial separation of Al and O ions).

distance for the heat wave propagation is a solution for the following equations:

$$\left(\frac{r}{r_0}-1\right)^2\left(\frac{r}{r_0}\right)^{15/2}=\frac{t}{t_0},$$
$$t_0=\frac{r_0^2}{2.67\ (k_{\mathrm{B}}T_{\mathrm{e}}/10\,\mathrm{eV})^{5/2}}. \tag{19}$$

Taking $r_0 = r_{\mathrm{eff}} = 0.254\,\mu\mathrm{m}$, $T_0 = 50\,\mathrm{eV}$ one obtains the characteristic heat conduction time $t_0 = 4.3\,\mathrm{ps}$. The numerical solution for equation (19) at $t = t_0$ gives $r/r_0 \cong 1.34$. This means that the heat wave propagated 86 nm during this time, while the temperature decreased 2.4 times.

The light oxygen ion in silica and sapphire gets energy from the electrons earlier than the heavy ones. The time difference in the energy transfer between the lighter and heavier ions reads $t_{\mathrm{h}} - t_{\mathrm{l}}\,(\mathrm{s}) \cong 2\times10^{-16}(M_{\mathrm{l}}/m_{\mathrm{e}})(k_{\mathrm{B}}T_{\mathrm{e}}/10\,\mathrm{eV})^{3/2}\,(M_{\mathrm{h}}/M_{\mathrm{l}}-1)$. Thus the light ion (oxygen) starts moving ~4–45 ps earlier than the heavy ion (Al or Si). The spatial separation of the shock front created by the light ions from the one formed later by the heavy ions is equal to $\Delta x_{\mathrm{separation}} \approx v_{\mathrm{l}}\,(t_{\mathrm{h}} - t_{\mathrm{l}}) \propto M_{\mathrm{l}}^{1/2}\,T_{\mathrm{l}}^2\,(M_{\mathrm{h}}/M_{\mathrm{l}}-1)$. The shock front separation for the case of oxygen and Al (or Si) is in the span of 33–75 nm for the above-mentioned experimental parameters. The front of the shock wave has a peculiar structure: the electron heat wave creates a long 'beak' on the spatial profile, followed by light ions shock front and later by the heavy ions (see figure 4).

Further increase in the spatial separation of ions with different masses could be achieved at the cooling stage due to the differences in the diffusion velocities. The passage of the electronic heat wave into the laser-unaffected (cold) region produces at least a single ionization state by an electron impact. After the shock wave stopping an ion starts diffusing into a single-ionized plasma with average ion mass $M_{\rm av} = (M_0 + M_{\rm Al})/2$. We show above that the collision rate in the plasma created in confined microexplosion is approximately four times lower than that for the ideal plasma. Respectively, the mean free path shall be longer than in the ideal plasma.

One can see that the mean free paths for aluminium $l^{\rm Al}_{\rm mfp}$ and oxygen $l^{\rm O}_{\rm mfp}$ ions are comparable, because the difference in velocities is compensated for by the difference in the reduced mass. Therefore, the difference in the diffusion coefficients relates mainly to the different velocities. Taking $l^{\rm O}_{\rm mfp} \approx l^{\rm Al}_{\rm mfp} \approx 4 \times 10^{-7}$ cm, one obtains the diffusion coefficients as $D^{\rm O}_{\rm diff} = 0.32\,{\rm cm}^2\,{\rm s}^{-1} =$ and $D^{\rm Al}_{\rm diff} = 0.248\,{\rm cm}^2\,{\rm s}^{-1}$. Further separation of oxygen and aluminium is achieved due to the difference in diffusion velocities during the cooling time of approximately 100 ps after the pulse. Thus the total separation on the shock wave formation stage plus that at the diffusion stage amounts to 40–80 nm, sufficient for the formation of the aluminium nanocrystals. At present we have no experimental information on the location of oxygen after the sample cools down to the ambient conditions. One of the possible routes is the formation of oxygen-rich radicals $Al_xO_y^-$ ($x = 2$, $y = 4$–5) around the laser- and shock-wave-affected areas [23].

6. Microexplosion experiments

Experimental studies of ionization wave propagation require precise positioning of the laser energy deposition in confined microexplosion conditions. This was resolved by using a Si-wafer with a thermally oxidized transparent SiO_2 layer on the surface as a target. The thermal oxidation process consists of exposing the silicon substrate to an oxidizing environment of water vapour cycled with oxygen oxidation at ~1000–1200 °C to produce a high-quality homogeneous film of silicon oxide on the surface. We have chosen the thickness of the SiO_2 layer to be 10 μm, which is not so deep to develop large spherical aberrations with high-NA focusing optics and at the same time guarantee the intensity on the surface well below $10^{12}\,{\rm W\,cm}^{-2}$ to avoid optical breakdown. The thickness of the boundary between the transparent oxidized layer and crystalline Si where the laser radiation is focused is of the order of only 2 nm, as can be clearly seen in electron microscope images.

The experiments were conducted with 170 fs, 790 nm, laser pulses from the MXR-2001 CLARK laser system. Pulses with up to 2.5 μJ per pulse were focused using an optical microscope (Olympus IX70) equipped with an oil-immersion $\times 150$(NA = 1.45) and dry $\times 20$(NA = 0.45) objective on a Si surface buried under a 10 μm-thick SiO_2 layer. The focal spots were measured using a knife-edge technique with a sharp edge of a Si ⟨100⟩ wafer etched at 54.74° to the surface along the ⟨111⟩ direction and mounted on a nano-positioning stage. The focal spots were measured to have radii of $r_{\rm f} = 0.368$ and 1.7 μm at the full-width at half-maximum level with correspondingly $\times 150$ and $\times 20$ objectives. The experiments were conducted with laser pulses at 1 kHz repetition rate in a sample moved at a rate $2\,{\rm mm\,s}^{-1}$ to guarantee a single shot per spot regime, so that each of the shots was located 2 μm apart.

The voids and shock wave modified areas of Si/SiO_2 sandwich were milled and opened up from a bulk using a focused-ion beam (FIB) and then characterized by scanning and transmission electron microscopy (SEM and TEM). Each of the regions irradiated by a single

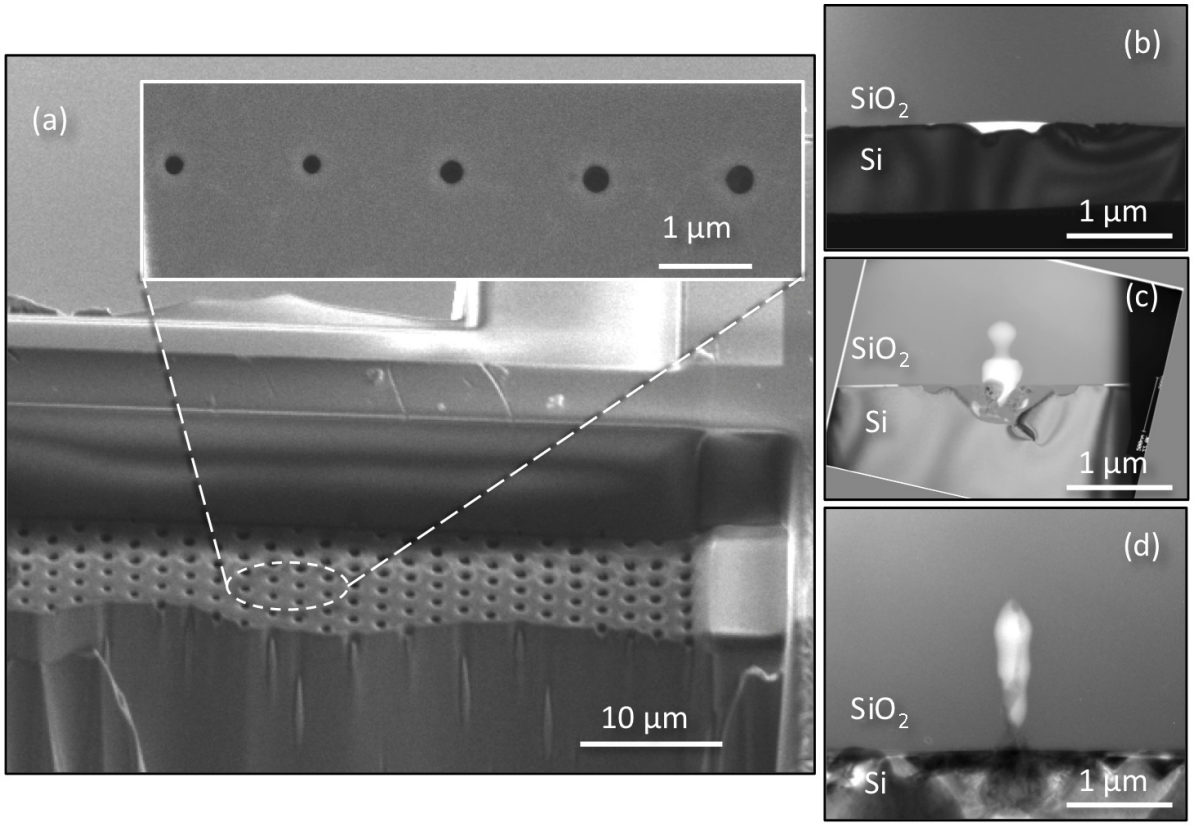

Figure 5. Electron microscope images of laser produced voids beneath the SiO_2 surface of the oxidized wafer. (a) SEM image of FIB-opened section showing an array of voids produced by 170 fs, 800 nm, 300 nJ single laser pulses focused 2 μm apart with $\times$150 objective; the inset shows a magnified transverse cross-section of voids. (b)–(d) TEM side views of voids at the Si/SiO_2 interface produced by single 400 nJ pulses focused with $\times$20 objective to 2 J/ cm^{-2} (c) and with $\times$150 objective focused at 42 J cm^{-2} (c) and 95 J cm^{-2} (d). The TEM images (b)–(d) demonstrate the elongation of voids toward the laser pulse with an increase of laser fluence, starting from the $Si–SiO_2$ interface at 2 J cm^{-2} just above the threshold of optical breakdown.

laser pulse at fluence above $\sim$1 J cm^{-2} contains a void located at the focal spot. Examples of typical SEM and TEM images of the voids are presented in figure 5. The elongation of voids towards the laser beam with an increase of laser fluence was clearly observed in TEM images. The thermal wave and shock wave after the pulse are responsible for a clearly seen affected area of Si crystal below the void. Studies of the modified structure will be presented elsewhere. The ionization front propagation was measured as the distance from the Si/SiO_2 interface to the top of the void formed in glass at various fluences and plotted in graphs in figure 6 together with the ionization time determined using equations (13) and (14).

Simple geometrical considerations of equations (13) and (14) are in qualitative agreement with experiments. Indeed, the laser pulses (170 fs, 800 nm) were focussed with NA = 1.45 ($\alpha = 75.2^\circ$; $\tan\alpha = 3.78$) inside silica to the focal spot with $r_f = 0.365\ \mu$m ($F_{max} = 95$ J cm^{-2}).

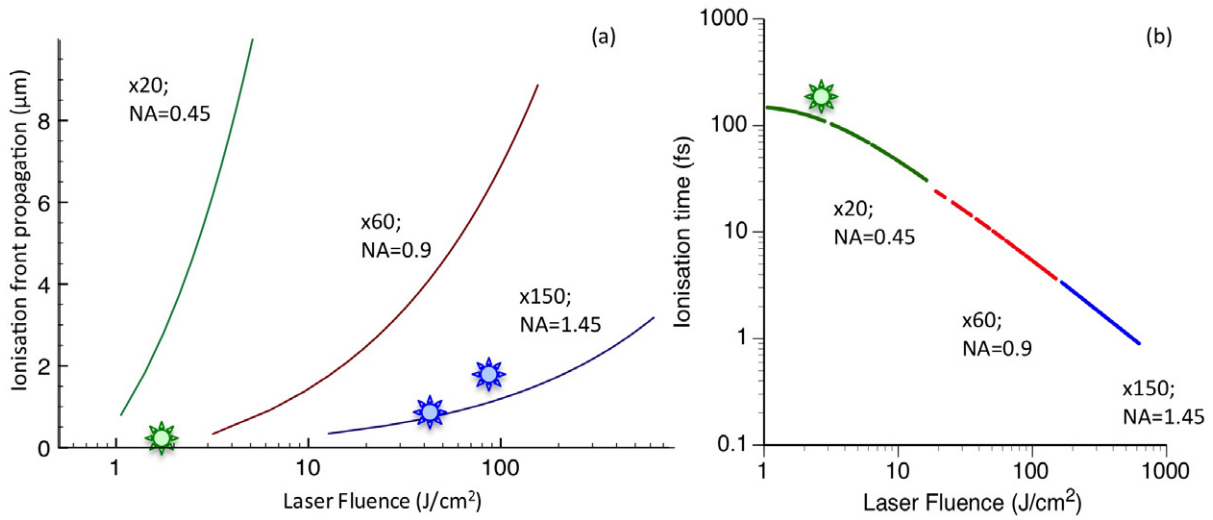

Figure 6. Calculated ionization front propagation (a) and ionization time (b) dependences on laser fluence for 170 fs laser pulses. The experimental points in (a) at 2 J cm^{-2} with ×20 objective, and at 42 and 95 J cm^{-2} with ×150 objective show qualitative agreement with geometrical estimates equations (13) and (14). The experimental point in (b) is from [21].

The ionization threshold for fused silica is equal to $F_{\rm thr} = 1.87\,{\rm J\,cm^{-2}}$ [18, 19, 21], resulting in $f = 51$. With the help of equation (13) one obtains that the ionization front during the pulse moves to the distance $z_{\rm max} = 600\,{\rm nm}$, which is in close agreement with the observed elongation of the voids $\sim 1\,\mu{\rm m}$. The movement of the ionization front towards the laser pulse due to optical breakdown provides a reason for the observed tear-like shape of voids formed by ultrashort laser pulses in transparent dielectrics [7–10].

Let us now analyse the results. A material should be removed from the energy deposition region in order to form a void. Therefore, the observation of a large void is unequivocal evidence of creation of the pressure well in excess Young's modulus of both materials, $Y_{\rm SiO_2} \sim 75\,{\rm GPa}$ for SiO_2 and $Y_{\rm Si} \sim 65\,{\rm GPa}$ for Si. In order to comply with the mass conservation the removed material should form a compressed shell at the void periphery. However, it was difficult distinguishing between laser-affected and pristine materials in SEM images. The shock wave stops when the pressure behind the shock front is comparable to the strength of the material. It means that all absorbed energy behind the surface where the shock stops created a pressure comparable with the strength of the surrounding material. At this point the shock wave converts into a sound wave, which propagates further into the material without inducing any permanent changes. One can see from figure 5 that 300 nJ of absorbed energy produces a void in fused silica with the size 300–400 nm in the transverse cross-section. In the z-direction the voids produced with 200 nJ are $\sim 0.6\,\mu{\rm m}$ and with 400 nJ are 1.1–1.4 μm. The results of the average size of the voids at various laser energies are presented in figure 7. The average size was calculated by approximating the void volume by an ellipse with the axis lengths measured as the void radius and the elongated size, and taking a cubic root of the resulting volume. Indeed, $E_{\rm abs} = 4\pi r_{\rm stop}^3 Y_{\rm SiO_2}/3$ [9], taking $E_{\rm abs} \sim 300\,{\rm nJ}$ and $Y = 75\,{\rm GPa}$ one obtains $r_{\rm stop} \sim 2\,\mu{\rm m}$, reasonably close to that observed in experiments.

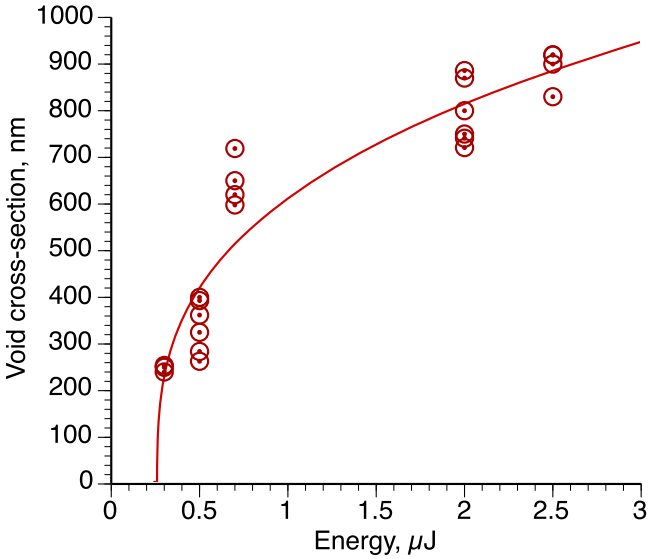

Figure 7. The average size of the voids (the cubic root of the void volume) produced by 170 fs pulses at the Si/SiO_2 interface. The solid curve is a fitting $r \propto E_{abs}^{1/3}$ according to [9].

7. Conclusions

Let us summarize briefly the results of this study. A major advance presented in this work is the demonstration, both theoretically and in experiments, that the process of ionization takes time, which depends on the absorbed laser fluence. We demonstrate that a laser pulse with a fluence up to 50 times above the ionization threshold with intensity up to 5×10^{15} W cm^{-2} can be efficiently absorbed in the focal area in the bulk of the transparent material. We also found the relations between the ionization thresholds and Young's modulus of the material, which should be maintained in order to maximize the absorbed energy density in the bulk.

Our studies of laser beam propagation in a transparent solid demonstrated that the increasing ionization rate might affect the magnitude of the absorbed energy density. At low intensity when the real part of the dielectric function slightly decreases, these effects comprise defocusing, blue shift of the pulse spectrum and an initial increase in the group velocity of the beam previously observed in the breakdown of gases [14]. Further increase in intensity and in the ionization rate leads to a sharp decrease in the real part of the dielectric function and group velocity, resulting in effective wave stopping and energy absorption at the breakdown spot. The most important outcome is the effect of the motion of the ionization front in the direction opposite to the laser pulse propagation. This effect is especially pronounced when the total absorbed fluence significantly exceeds the ionization threshold of the material. The absorption volume and therefore the laser-affected volume became elongated, as clearly observed experimentally by the elongation of voids in the direction of the laser axis.

In earlier studies the effect of spatial separation of both light and heavy ions in hot and dense plasma was found to be responsible for the formation of new crystals of bcc-Al [12]. Here we found that the plasma created by microexplosion is in fact in the non-ideal state where the Coulomb interactions dominate. The electron–ion collision rate in non-ideal plasma appears

to be lower than that for the ideal plasma leading to an increase in the separation distance of the ions with different masses.

Summing up, the possibility to generate sub-TPa pressure has already been demonstrated. In future studies we plan to generate TPa pressures on confined microexplosion in the materials with a high Young's modulus such as silicon carbide and diamond, to perform experiments with materials with a large difference in mass such as, for example, lead fluoride (PbF_2), to expand the studies of structural modification to opaque materials buried under the transparent layers, and to develop the pump–probe technique for observing the *in situ* process of the microexplosion in real time with fs-temporal resolution.

Acknowledgments

The authors are grateful to W Krolikowski for many helpful discussions and to B Haberl and J E Bradby for their help with TEM images. This work was supported by the Australian Research Council's Discovery Projects funding scheme (project number DP110100975).

References

[1] McMillan P F 2002 New materials from high-pressure experiments *Nature Mater.* **1** 19–25
[2] Ahrens T 1980 Dynamic compression of earth materials *Science* **207** 1035–41
[3] Drake R P 2010 High-energy-density physics *Phys. Today* **63** 28–33
[4] Salleo A, Taylor S T, Martin M C, Panero W R, Jeanloz R, Sands T and Genin F Y 2003 Laser-driven formation of a high-pressure phase in amorphous silica *Nature Mater.* **2** 796–800
[5] Cauble R, Phillion D W, Hoover T J, Holmes N C, Kilkenny J D and Lee R W 1993 Demonstration of 0.75 Gbar planar shocks in x-ray driven colliding foils *Phys. Rev. Lett.* **70** 2102–5
[6] Glezer E and Mazur E 1997 Ultrafast-laser driven micro-explosions in transparent materials *Appl. Phys. Lett.* **71** 882–4
[7] Juodkazis S, Misawa E, Gamaly H, Luther-Davies L, Hallo B, Nicolai P and Tikhonchuk V T 2006 Laser-induced micro-explosion inside of sapphire crystal: evidence of multi-megabar pressure *Phys. Rev. Lett.* **96** 166101
[8] Juodkazis S, Misawa H, Hashimoto T, Gamaly E and Luther-Davies B 2006 Laser-induced micro-explosion confined in a bulk of silica: formation of nano-void *Appl. Phys. Lett.* **88** 201909
[9] Gamaly E G, Juodkazis S, Misawa H, Luther-Davies B, Hallo L, Nicolai P and Tikhonchuk V T 2006 Laser–matter interaction in a bulk of a transparent solid: confined micro-explosion and void formation *Phys. Rev.* B **73** 214101
[10] Bressel L, de Ligny D, Gamaly E G, Rode A V and Juodkazis S 2011 Observation of O_2 inside voids formed in GeO_2 glass by tightly-focused fs-laser pulses *Opt. Mater. Express* **1** 1150–7
[11] Juodkazis S, Kohara S, Ohishi Y, Hirao N, Vailionis A, Mizeikis V, Saito A and Rode A V 2010 Structural changes in femtosecond laser modified regions inside fused silica *J. Opt.* **12** 124007
[12] Vailionis A, Gamaly E G, Mizeikis V, Yang W, Rode A V and Juodkazis S 2011 Evidence of superdense aluminium synthesized by ultrafast microexplosion *Nature Commun.* **2** 445
[13] Raizer Yu P 1978 *Laser-Induced Discharge Phenomena* (New York: Consultant Bureau)
[14] Luther-Davies B, Gamaly E, Wang Y, Rode A and Tikhonchuk V 1991 Interaction of ultra-short powerful laser beam with matter *Laser Phys.* **1** 325–65
[15] Rayner D M, Naumov A and Corkum P B 2005 Ultrashort pulse non-linear optical absorption in transparent media *Opt. Express* **13** 3208–17
[16] Il'inskii Yu A and Keldysh L V 1994 *Electromagnetic Response of Material Media* (New York: Springer)

[17] Gamaly E G 2011 *Femtosecond Laser–Matter Interaction: Theory, Experiments and Applications* (Singapore: Pan Stanford Publishing)
[18] Stuart B C, Feit M D, Rubenchick A M, Shore B W and Perry M D 1995 Laser-induced damage in dielectrics with nanosecond to picosecond pulses *Phys. Rev. Lett.* **74** 2248–51
[19] Stuart B C, Feit M D, Herman S, Rubenchik A M, Shore B W and Perry M D 1996 Optical ablation by high-power short-pulse lasers *J. Opt. Soc. Am.* B **13** 459–68
[20] Zel'dovich Ya B and Raizer Yu P 2002 *Physics of Shock Waves and High-Temperature Hydrodynamic Phenomena* (New York: Dover)
[21] Temnov V V, Sokolowski-Tinten K, Zhou P, El-Khamhawy A and von der Linde D 2006 Multiphoton ionization in dielectrics: comparison of circular and linear polarization *Phys. Rev. Lett.* **97** 237403
[22] Kruer W L 1988 *The Physics of Laser Plasma Interactions* (New York: Addison-Wesley)
[23] Desai S R, Wu H, Rohlfing C M and Wang L-S 1997 A study of the structure and bonding of small aluminium oxide clusters by photoelectron spectroscopy: $Al_xO_y^-$ ($x = 1$–2, $y = 1$–5) *J. Chem. Phys.* **106** 1309–17